Damage Curves Derived from Hurricane Ike in the West of Galveston Bay Based on Insurance Claims and Hydrodynamic Simulations

Xu, Chaoran; Nelson-Mercer, Benjamin T.; Bricker, Jeremy D.; Davlasheridze, Meri; Ross, Ashley D.; Jia, Jianjun

DOI
10.1007/s13753-023-00524-8

Publication date
2023

Document Version
Final published version

Published in
International Journal of Disaster Risk Science

International Journal of Disaster Risk Science
https://doi.org/10.1007/s13753-023-00524-8

www.ijdrs.com
www.springer.com/13753

ARTICLE

Damage Curves Derived from Hurricane Ike in the West of Galveston Bay Based on Insurance Claims and Hydrodynamic Simulations

Chaoran Xu[1,2] · Benjamin T. Nelson-Mercer[2] · Jeremy D. Bricker[2,4] · Meri Davlasheridze[3] · Ashley D. Ross[3] · Jianjun Jia[1]

Accepted: 10 December 2023

Abstract
Hurricane Ike, which struck the United States in September 2008, was the ninth most expensive hurricane in terms of damages. It caused nearly USD 30 billion in damage after making landfall on the Bolivar Peninsula, Texas. We used the Delft3d-FM/SWAN hydrodynamic and spectral wave model to simulate the storm surge inundation around Galveston Bay during Hurricane Ike. Damage curves were established through the relationship between eight hydrodynamic parameters (water depth, flow velocity, unit discharge, flow momentum flux, significant wave height, wave energy flux, total water depth (flow depth plus wave height), and total (flow plus wave) force) simulated by the model and National Flood Insurance Program (NFIP) insurance damage data. The NFIP insurance database contains a large amount of building damage data, building stories, and elevation, as well as other information from the Ike event. We found that the damage curves are sensitive to the model grid resolution, building elevation, and the number of stories. We also found that the resulting damage functions are steeper than those developed for residential structures in many other locations.

Keywords Delft3d-FM · Flood risk · Hurricane Ike · Residential damage ratio · SWAN · Weibull function

1 Introduction

Hurricanes are highly destructive marine weather systems that are accompanied by gale-force winds, heavy rainfall, and storm surges (Muis et al. 2016). This can result in low-latitude coastal zones at lower elevations being highly susceptible to flooding (Tyler et al. 2021). It is estimated that 10% of the world's population lives in the 2% of the total landmass of the Earth that comprises the low-elevation coastal zone, which is vulnerable to storm surge and inundation (Oliver-Smith 2009). In the United States, hurricanes have been responsible for eight of the top 10 costliest disasters since the 1980s (NOAA 2023); globally, the annual hurricane damage is about USD 26 billion (Mendelsohn et al. 2012). Meanwhile, because of global warming, more warm and wet seawater evaporates to increase the moisture in the air, which leads to an increase in the intensity of hurricanes and slowing of onshore storm weakening, so coastal areas may suffer more economic losses in the future (Knutson et al. 2019; Li and Chakraborty 2020; Xu, Yang, et al. 2022). Storm surge is a major driver of food risk, and coastal development also magnifies risk by increasing exposure to these hazards (Davlasheridze et al. 2019; Reed et al. 2020; Davlasheridze et al. 2021; Törnqvist et al. 2021). The East Coast and Gulf Coast of the United States are regions heavily affected by storm surges, aggravated by global warming; on these flat floodplains, the risk of storm surges can extend several miles inland from the coast, depending on topography, hurricane intensity, and tidal levels during the hurricane (Al-Attabi et al. 2023).

Coastal planners need methods to reduce the damage to residences during hurricanes, and the critical first step is predicting the relationship between damage and environmental

✉ Jeremy D. Bricker
jeremydb@umich.edu

1 State Key Laboratory of Estuarine and Coastal Research, School of Marine Sciences, East China Normal University, Shanghai 200241, China

2 Department of Civil and Environmental Engineering, University of Michigan, Ann Arbor, MI 48109, USA

3 Department of Marine and Coastal Environmental Science, Texas A&M University at Galveston, Galveston, TX 77553, USA

4 Faculty of Civil Engineering and Geosciences, Delft University of Technology, 2628 CN Delft, The Netherlands

Published online: 20 December 2023

and structural variables. Common environmental forcings associated with hurricane damage include water depth and flow velocity (Tomiczek et al. 2017). The damage curve of a building is influenced by its structural features, such as the building material, construction methods, codes, and layout, including the distance between buildings (Suppasri et al. 2013; Huizinga et al. 2017; Masoomi et al. 2019; Postacchini et al. 2019; Jansen et al. 2020). Damage curves are often used to parameterize this relationship and are an important tool for risk assessment related to environmental and structural vulnerability (Pistrika and Jonkman 2009; Englhardt et al. 2019). Damage curves have been widely applied in the United States, Europe, and Japan (Suppasri et al. 2013; Tomiczek et al. 2017; Hatzikyriakou and Lin 2018; Diaz-Loaiza et al. 2022). Suppasri et al. (2013) established damage curves for Japanese coastal zones based on flood depths for residential structures (including the number of residential floors and the type of residential construction materials). Tomiczek et al. (2017) studied the relationship between structural damage state and flow velocity in New Jersey as a result of Hurricane Sandy. However, these studies focused only on a single variable. The National Flood Insurance Program (NFIP) provides a large amount of measured insurance claims data including water depth, the amount of residential damage, the number of residential floors, and other residential information (FEMA 2023). In the United States, widely used curves have been compiled by the Army Corps of Engineers (USACE) based on NFIP data. However, there are anomalies in the NFIP water depth data, so damage curves based on these lack reliability (Wing et al. 2020).

The rapid evolution of flood hazard modeling techniques, fueled by advances in computer power and the development of high-resolution terrain data, has brought about a transformative shift in our understanding of flood hazard, even at continental and global scales (Sampson et al. 2015; Winsemius et al. 2015). While water depth is an important variable as it reflects the static forces exerted on a structure, in hurricane events, structures located near the coast may also be subjected to dynamic forces, such as the impact of flow and waves (Kreibich et al. 2009; Tomiczek et al. 2017). Therefore, flood damage is not only related to the water depth and flow velocity, but six other hydrodynamic parameters (unit discharge, flow momentum flux, significant wave height, total water depth, wave energy flux, and total force) are also very significant (Tsubaki et al. 2016; Bricker et al. 2017; Diaz-Loaiza et al. 2022). However, few studies have been done in this area to provide more perspective on flood risks in coastal zones (Kreibich et al. 2009; De Risi et al. 2017; Jansen et al. 2020). Hurricane Ike (2008) caused about USD 30 billion in damage, of which insured losses amounted to USD 12.5 billion, and casualties around Galveston Bay, where strong onshore winds and low atmospheric pressure generated unprecedented inundation (Veeramony et al. 2016). Therefore, the establishment of damage curves with eight hydrodynamic parameters in this region is important for future disaster mitigation. In this study, we applied the Delft3d-FM numerical model to obtain more accurate hydrodynamic parameters, and through the NFIP database had access to over 20,000 residential claims associated with Hurricane Ike. Therefore, the main objective of the present study was to develop damage curves from NFIP insurance claims data supported by hydrodynamic modeling during Hurricane Ike.

2 Methods

This section begins with an overview of the study area and hurricane Ike. It then covers data sources, introduces the Delft3D-FM, discusses model validation, and outlines the method for damage curve generation.

2.1 Study Area and Hurricane Ike

Galveston Bay is a densely populated, hurricane-prone region. The bay is 50 km long and 27 km wide and is the largest estuary along the Gulf Coast of Texas with a surface area of 1554 km^2. Galveston Bay is shallow, with an average water depth of 3 m, but has a shipping channel of 12 m depth. The San Jacinto and Trinity Rivers are the main sources of fresh water into the bay. On the ocean side, two entrances connect the bay with the Gulf of Mexico (Al-Attabi et al. 2023). Hurricane Ike made landfall between Galveston Island and the Bolivar Peninsula (Fig. 1) on 10 September 2008, with sustained wind speeds of 130–148 km/h and a surge of 5 m on the Bolivar Peninsula; sustained wind speeds of 120–130 km/h and a surge of 3.5 m on Galveston Island (Overpeck 2009; Sebastian et al. 2014). Although it had weakened to a Category 2 storm when it made landfall, its strong wind field caused a large storm surge in Galveston Bay, causing severe flooding hazards and major destruction of coastal properties. Hurricane Ike directly caused about USD 30 billion in damage and 12 fatalities in this region (Berg 2009). Since most of the population is concentrated on the western shore of the bay and the east is mostly coastal wetlands, the economic loss on the west shore is greater than that on the east shore (Al-Attabi et al. 2023). Therefore, this study focused on the western region of Galveston Bay and established damage curves for the western shore of the bay (Fig. 1).

2.2 Hydrodynamic Model of Hurricane Ike

This section introduces the data sources, Delft3D-FM model, and its settings, and presents validation results.

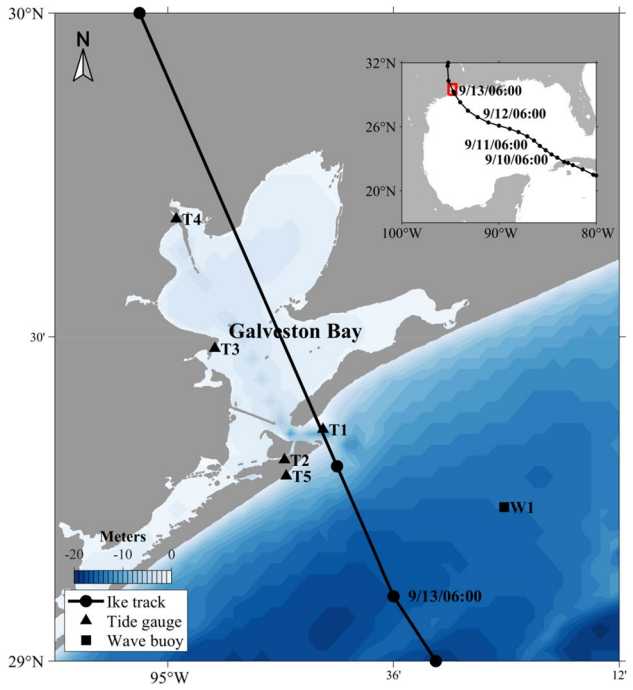

Fig. 1 The study area and track of Hurricane Ike. The inset figure is the Gulf of Mexico, and the red box is the study area, T1–T5 (black triangles) are the tide gauges, and W1 (black square) is the wave buoy.

2.2.1 Data Sources

We used two topography datasets: a global dataset for the bathymetry (GEBCO2022, 15-arc seconds) for the deep sea, and a high-resolution bathymetry (ETOPO2022, 1-arc second) for Galveston Bay and inland. Astronomical tides (K1, O1, Q1, P1, M2, S2, N2, and K2) on the open boundaries applied harmonics from the OTIS regional and global tidal models (Egbert and Erofeeva 2002). To study the impact of flooding overland, the land roughness was represented in the model with Manning coefficients. Coefficient values are based on the land cover classifications obtained from the 2019 National Land Cover Database (NLCD).[1] The land cover classifications were transformed into the corresponding Manning's n values based on Bunya et al. (2010). The hurricane track data used in this study were obtained from the Atlantic Hurricane database (HURDAT2), which contains the time, latitude, longitude, central minimum pressure, and central maximum wind speed of the hurricane eye (Franklin and Landsea 2013). The radius to maximum winds from the Tropical Cyclone Extended Best Track Dataset (EBTRK) (Demuth et al. 2006) supplemented this dataset. Measured water level, significant wave height, wave peak period, wind speed, and pressure values used in the model validation of this study are all from NOAA Tides and Currents.[2] We used more than 20,000 flood damage claims from the NFIP during Hurricane Ike. These data were obtained from the Institute for a Disaster Resilient Texas and include the number of stories, elevated building indicator, building claim payment, replacement cost, latitude, and longitude of each claim. The model input files can be downloaded at http://deepblue.lib.umich.edu/data/concern/data_sets/8049g586z.

2.2.2 Hurricane Model

The accuracy of the simulated storm surge model is primarily contingent upon the precision of external forcing factors, particularly the wind field and the reduction in barometric pressure. Delft3D Wind Enhanced Scheme (WES), an integrated module within the Delft3D, utilizes the Holland formula (Holland 2008; Holland et al. 2010) and the radius of maximum winds relation formula (Nederhoff et al. 2019) based on hurricane data (the HURDAT2 hurricane database was used in this study) to produce wind and air pressure fields for each hurricane. It is capable of generating hurricane wind and pressure fields around the storm eye positions on a high-resolution grid. Delft3D WES incorporates asymmetry by taking into account the translational speed of the cyclone center's displacement by the steering flow, as well as the rotation of wind velocity due to friction (Takagi and Wu 2016). The Delft3D WES output is appropriate for utilization as input in the D-Flow FM model, enabling the simulation of flow and wave patterns, as well as the impact of storm surges. The wind and pressure fields generated by WES were validated against observations from a NOAA tidal station in Galveston Bay (Fig. 1, T3). Three accuracy indicators: the root mean square error (RMSE, Eq. 1), the relative root square error (RRSE, Eq. 2), and the Pearson correlation coefficient (ρ, Eq. 3) are assessed to validate the model.

$$\mathrm{RMSE} = \sqrt{\frac{\sum_{i=1}^{T}\left(y_i' - y_i\right)^2}{T}}, \tag{1}$$

$$\mathrm{RRSE} = \sqrt{\frac{\sum_{i=1}^{T}\left(y_i' - y_i\right)^2}{\sum_{i=1}^{T}\left(y_i - \bar{y}\right)^2}}, \quad \bar{y} = \frac{\sum_{i=1}^{T} y_i}{T} \tag{2}$$

[1] https://doi.org/10.5066/P9KZCM54.

[2] https://tidesandcurrents.noaa.gov/.

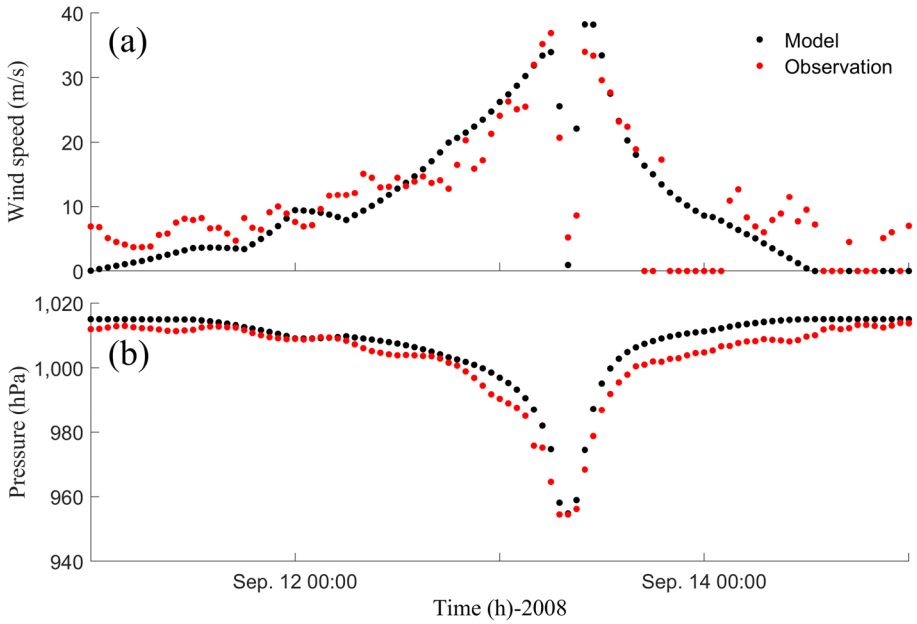

Fig. 2 Validation of the hurricane model at T3. **a** Wind speed validation; **b** pressure validation

$$\rho_{y,y'} = \frac{\mathrm{cov}\left(y_i, y_i'\right)}{\sigma_y \sigma_{y'}}, \tag{3}$$

where y' is the model result, y is the observation data and $\bar{y}$ is the average of the observation data, T is the number of data points, and σ indicates the standard deviation. The model results for wind speed exhibited strong agreement with the observation data; RMSE, RRSE, and ρ are 5.6 m/s, 0.83, and 0.84 respectively. The model pressure field also displayed a robust correlation with the observed data; RMSE, RRSE, and ρ are 3.3 hPa, 0.31, and 0.97 respectively (Fig. 2).

2.2.3 Flow and Wave Model Setup

Delft3D Flexible Mesh suite model solves the nonlinear shallow water equations for unsteady flow derived from the three-dimensional Navier-Stokes equations for incompressible free surface flow (Deltares 2022a). A dynamic time step is adopted whereby the model specifies the time step for each computational step to help maintain model stability and performance in this model. It also integrates the third generation wave model Simulating WAves Nearshore (SWAN), which is a spectral wave model used to solve the wave action balance equation. Delft3D can simulate tidal circulation and the propagation of storm surges in intricate coastal settings and is extensively applied in the modeling of flow and waves during hurricanes (Veeramony et al. 2016; Zou et al. 2020; Ke et al. 2021; Diaz-Loaiza et al. 2022; Xu, Tian et al. 2022; Al-Attabi et al. 2023).

The domain of the flow model covers the northwest of the Gulf of Mexico, roughly ranging from 22°N to 32°N and − 98°W to − 86°W (Fig. 3a, b). The grid is further resolved to a grid resolution of about 100 m landward of a line about 5 km offshore, extending to the western part of Galveston Bay, and consists of 180,000 cells. We used a high-resolution bathymetry of 1 arc-second in Galveston Bay and 15 arc-seconds in other regions. We added a 6 m high fixed weir (when the water level exceeds 6 m, the seawater can overflow this fixed weir and flood the land behind it) in the northeastern part of Texas City to represent a seawall in this region. Astronomical tides on the open boundaries applied harmonics from the OSU Tidal Inversion Software (OTIS) regional and local tidal models. A spatially varying Manning's coefficient derived from NLCD was applied to this model. The hurricane model calculated from WES acts as an external force to the model. The wind drag coefficients used in this model are from Makin (2005). The simulation was carried out for a period from 7 to 17 September 2008, the time step ranges from 1 s to 30 s and the other settings are kept as default.

The grids of the wave model are different from the flow model, using structured grids. There are three nesting domains in the wave model. The resolution of the large domain is about 5 km, covering the same spatial extent as the flow domain; the middle domain has a resolution of about 600 m, and covers the whole of Galveston Bay; there are three small domains, each of which has a resolution of about 100 m, and together cover the western part of Galveston Bay (Fig. 3c, d). The wave model grids consist of 201 × 151 cells in the large domain, 124 × 144 cells in the middle domain, and 251 × 201 cells, 171 × 201 cells, and 501 × 71 cells in the small domains. The time step is 60 min. The simulation mode is non-stationary. All the other settings

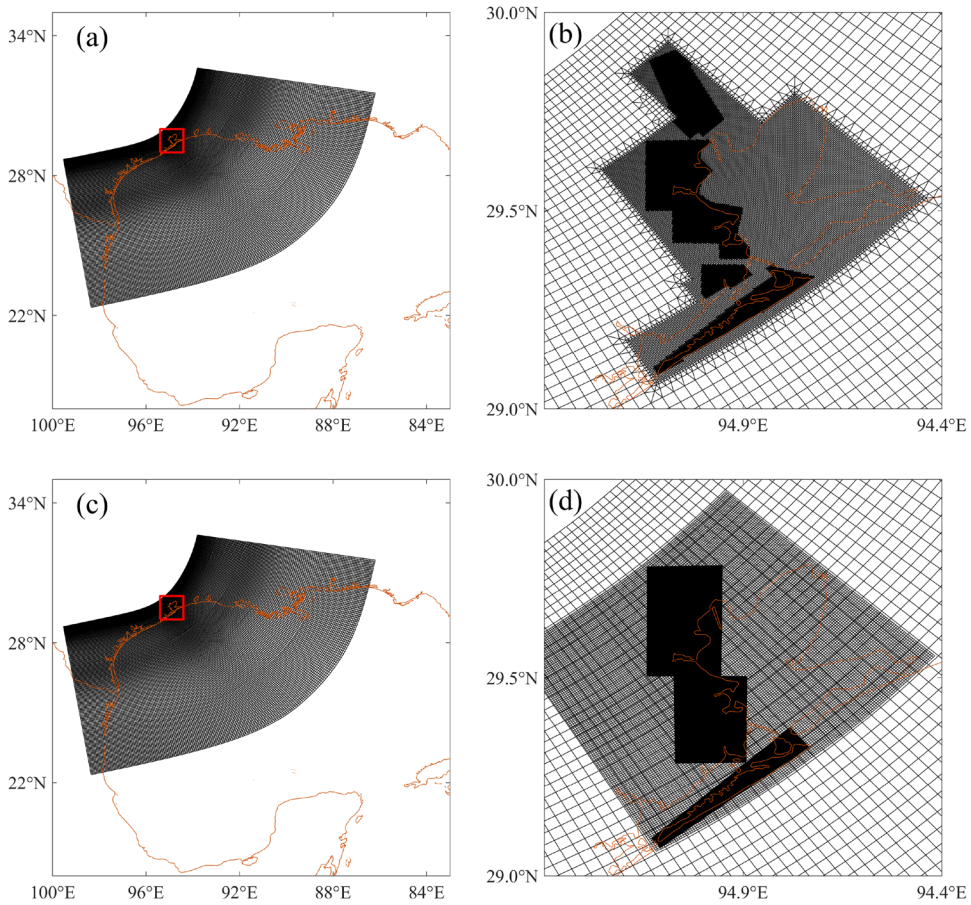

Fig. 3 Combination of triangular and curvilinear grids for the flow model and nested computational grid for the wave model. **a** The overall schematic of the grid, the red box is the study area where the grid is refined; **b** the refined area; **c** the coarse wave grid; **d** the middle and fine wave grid

of the wave model are kept as default (Deltares 2022b) and integrated with the flow model online. Flow and wave simulations exchange data every 60 min via a communication file, and the other input data are identical to those used in the flow model.

2.2.4 Flow and Wave Model Validation

We verified the accuracy of the integrated model from four aspects: flow water depth, wave height, peak wave period, and inundation water depth. Storm tide is validated against hourly water level data from NOAA tide gauges. Figure 4 shows good agreement between the observed and modeled water levels at T1–T5 (see tide gauge locations in Fig. 1) and the RMSE, RRSE, and ρ in Table 1 also indicate that they fit well. The wave model was validated against hourly significant wave heights and peak wave period from the NOAA wave buoy W1 (Fig. 4), and the observed and modeled values also fit well, as shown in Table 1. Assessment of the inundation in Galveston Bay is predominantly qualitative due to the lack of quantitative measurements of flood depth. An estimate of the observed inundation depth, presented by the Harris County Flood Control District (HCFCD 2009), is illustrated in Fig. 5a; the coast of Galveston Bay shows varying degrees of inundation. Figure 5b shows the simulated inundation, which can be seen to be consistent with the Harris County Flood Control District map. In summary, our model can simulate Hurricane Ike well.

2.3 Damage Curves

Damage curves are widely used to evaluate the vulnerability of buildings in terms of probability. Initially applied to evaluate seismic damage to bridges and structures (Shinozuka et al. 2000; Ichii 2002), the use of damage curves has been extended to water-related hazards as well (Zhang and Singh 2005; Suppasri et al. 2013; Tsubaki et al. 2016). In this study, damage curves were used to estimate the correlation between hydrodynamic parameters and damage ratio (DR) due to hurricanes. The hydrodynamic parameters are water depth (h), flow velocity (v), unit discharge (hv), flow momentum flux (ρhv^2), significant wave height (H), total water depth ($h + H$), wave energy flux (E), and total force ($\frac{E}{C} + \rho hv^2$). The wave energy flux is defined via Eq. 4:

$$E = \frac{1}{16}\rho g H^2 C \tag{4}$$

where C is the wave group velocity, ρ is the water density, g is the acceleration due to gravity, and $C = \sqrt{gh}$ in

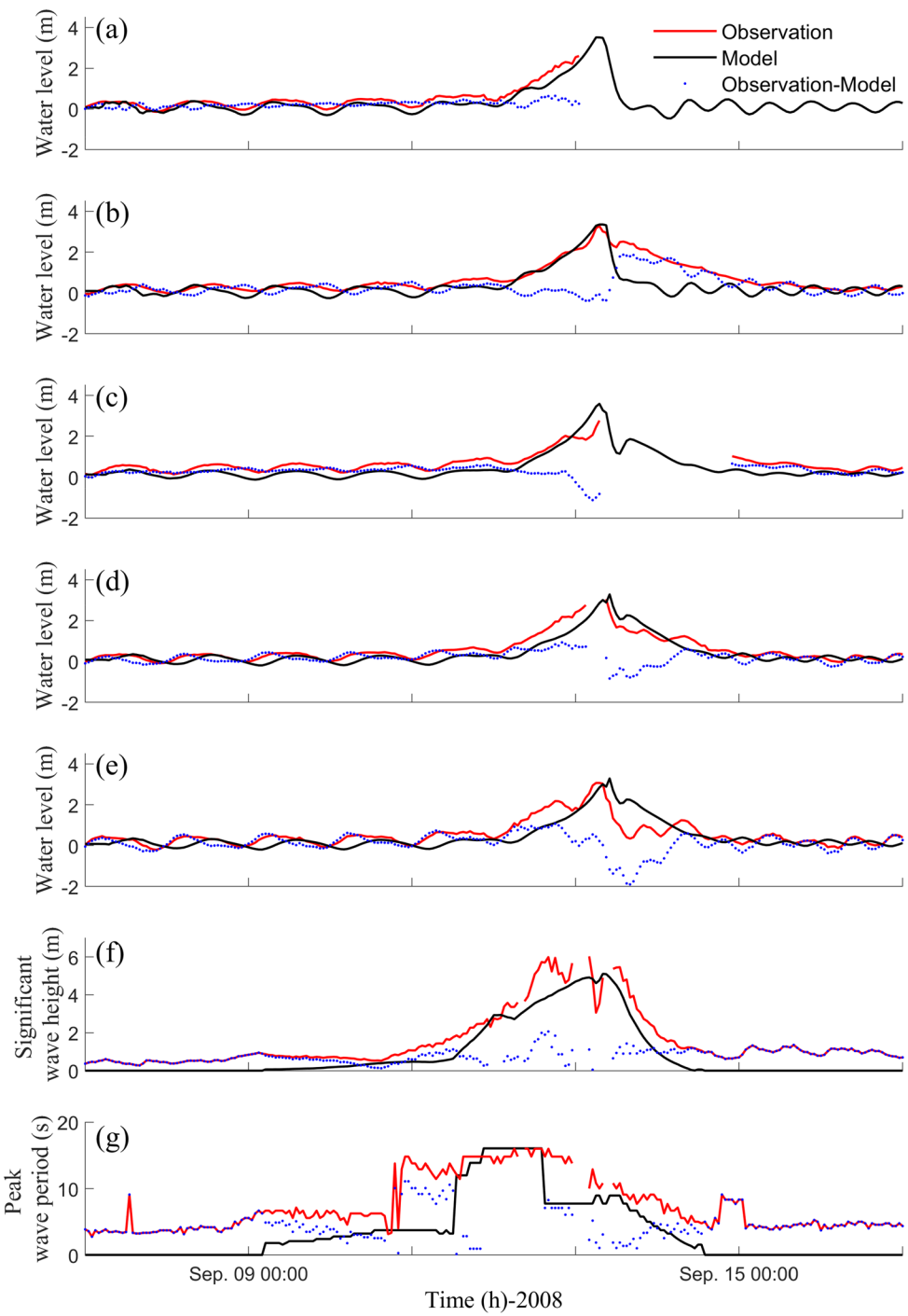

Fig. 4 Modeled versus observed water level, significant wave height, and peak wave period during Hurricane Ike. **a** Tide gauge T1 (8771341); **b** T2 (8771450); **c** T3 (8771013); **d** T4 (8770613); **e** T5 (8771510); **f** significant wave height and **g** peak wave period at buoy station W1 (42035)

shallow water. The DR in this study is defined as a claim payout divided by building replacement cost in the NFIP insurance database. The maximum value of each hydrodynamic parameter was extracted at each claim location, and the resulting data were used to compile the damage curves. A Weibull cumulative distribution function was used to fit the relationship between the two to derive the final damage curves (Zhang and Singh 2005; Totschnig and Fuchs 2013), as shown in Eq. 5.

$$P(x) = 1 - e^{-(x/\lambda)^{\kappa}} \tag{5}$$

where $P(x)$ is the cumulative probability of the DR with values between 0 and 1, x is the hydrodynamic parameter,

Table 1 Goodness of fit for water level and wave measurements compared with the results of the model

Station	RMSE	RRSE	ρ
T1	0.268 m	0.481	0.975
T2	0.570 m	0.793	0.773
T3	0.391 m	0.886	0.932
T4	0.341 m	0.575	0.882
T5	0.487 m	0.784	0.743
W1-1	0.842 m	0.596	0.956
W1-2	4.796 s	1.186	0.846

W1-1 is the significant wave height, and W1-2 is the peak wave period

RMSE root mean square error, *RRSE* relative root square error, and ρ is the Pearson correlation coefficient

Next, we present the extracted maximum values of hydrodynamic parameters on land and the constructed damage curves using both sets of data. Additionally, this section discusses the effect of building elevation and number of floors on the damage curves.

3.1 The Spatial Distribution of DR

The amount of building damage and replacement values for insured structures for western Galveston Bay from the 2008 hurricane Ike event were compiled by the NFIP and were used to calculate DR. From the histogram of DR (Fig. 6), about 20% of the structures had a DR higher than 0.5 (considerable damages), 20% had DR between

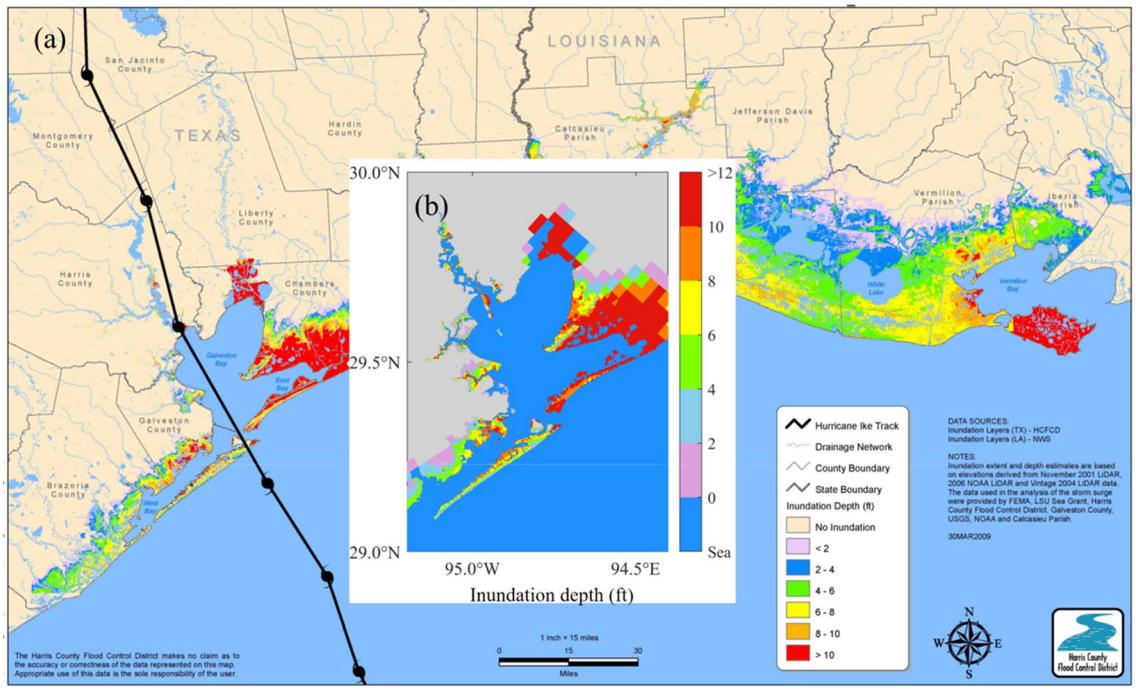

Fig. 5 Modeled versus observed inundation depth (ft) during Hurricane Ike. **a** Observed inundation depth, image from HCFCD (2009); **b** modeled maximum inundation depth

λ is the scale parameter, and κ is the shape parameter. In this study, the function parameters were assessed using the MATLAB Distribution Fitter application. This approach enables the establishment of a relationship between various hydrodynamic parameters and DR.

3 Results

This study aimed to establish damage curves linking hydrodynamic parameters with DR. In this section, we first present the results of calculating DR using NFIP data.

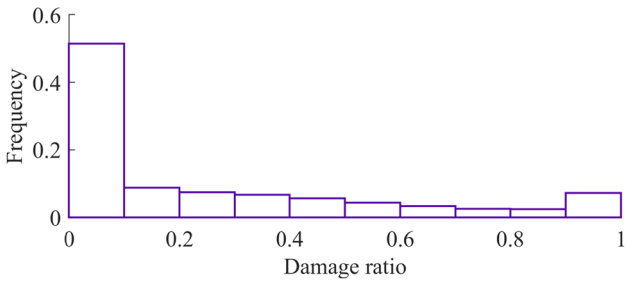

Fig. 6 Damage ratio histogram for insurance claims data in the western Galveston Bay region

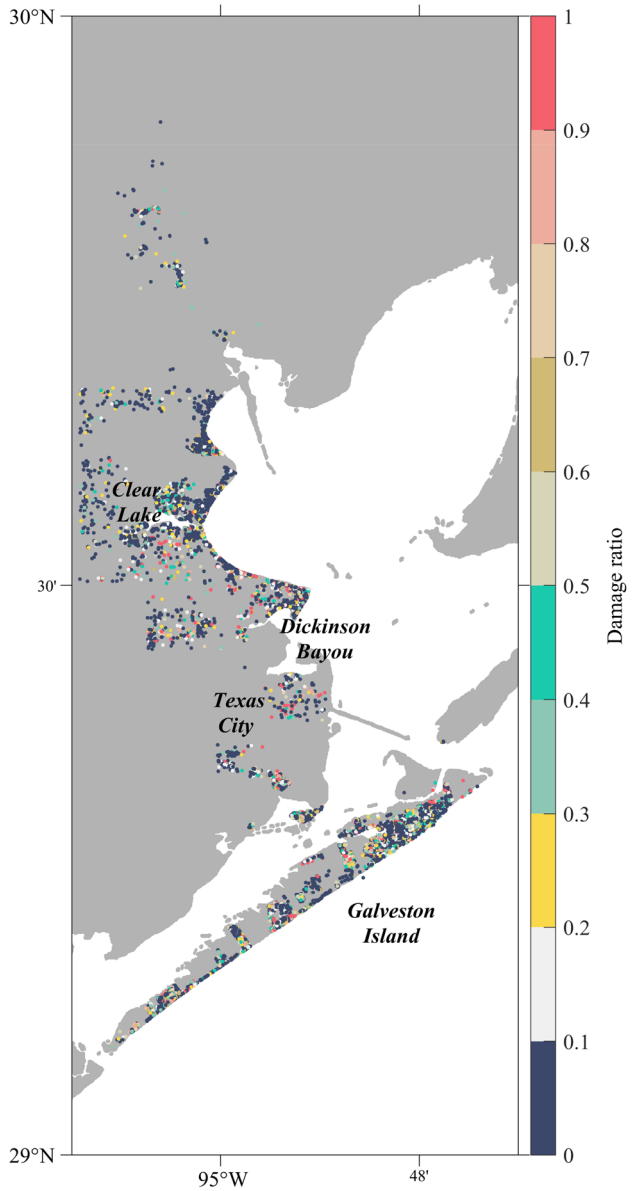

Fig. 7 Spatial distribution of DR in the western Galveston Bay region

0.2 and 0.5 (medium damage), and 60% had low damage (DR < 0.2). This is a typical distribution for damage claims (see for example Fuchs et al. (2019), Diaz-Loaiza et al. (2022)). From the spatial distribution of DR (Fig. 7), Galveston Island has high DR, followed by Clear Lake, and lower in Texas City and the northwest side of Galveston Bay.

3.2 Maximum Value of Each Hydrodynamic Parameter

After successfully obtained the DR data, we acquired the hydrodynamic parameter data. The water depth, velocity, and significant wave height were from the model directly, and unit discharge, flow momentum flux, total water depth, wave energy flux, and total force were calculated based on these three parameters (Bricker et al. 2017; Diaz-Loaiza et al. 2022). We then extracted the maximum values of these hydrodynamic parameters at each grid cell during Hurricane Ike (Fig. 8). The entire Galveston Bay largely suffers from varying degrees of seawater inundation, with the highest levels on the Bolivar Peninsula and Chambers County on the east side. There are five main areas of western Galveston Bay that are significantly affected. The entire Galveston Island on the southwest side is flooded and with the strongest hydrodynamic forces of the entire western area, followed by the mainland opposite Galveston Island. The Dickinson Bayou and Clear Lake coastal areas on the west also have strong hydrodynamic forces and most of the coastal areas are flooded. The northwestern bayou area has weaker hydrodynamic forces, with fewer areas flooded.

3.3 Damage Curves from Each Hydrodynamic Parameter

After determining the model flow and wave results at the location of each claim, we analyzed the relationship between the hydrodynamic data and DR data for each claim location to generate damage curves. There is a common method to build damage curves: group DR by hydrodynamic data and then use the cumulative frequency distribution function in Sect. 2.3 to fit to obtain the final damage curves (Suppasri et al. 2013; Tomiczek et al. 2017). Suppasri et al. (2013) used damage data grouped by water depth in building the damage curves during the 2011 tsunami in Japan, and the fit was good. We adopted this method and grouped the DR data according to water depth (0.3 m intervals), flow velocity (0.1 m/s intervals), unit discharge (1 m^2/s intervals), flow momentum flux (1 kg/s^2 intervals), significant wave height (0.1 m intervals), total water depth (0.5 m intervals), wave energy flux (50 kW/m intervals), and total force (50 N/m intervals) respectively. The relationship between hydrodynamic data and DR can be seen from the black dots in Fig. 9, where the DR gradually increases with the severity of the hydrodynamic hazard.

A comparison to three other typical distribution functions (normal, gamma, and log-normal) was also carried out (Fig. 9). It can be seen from Table 2 that the Weibull, normal, and gamma distributions have similar goodness-of-fit indicators, while the log-normal distribution performs slightly worse overall. Finally, combined with the fitted damage curves in Fig. 9, the Weibull distribution function fits better when the DR is below 0.7–0.8 and outperforms the normal and gamma functions overall. Therefore, the results of the fitted damage curves of the Weibull distribution function were used in the subsequent analysis of this study. We

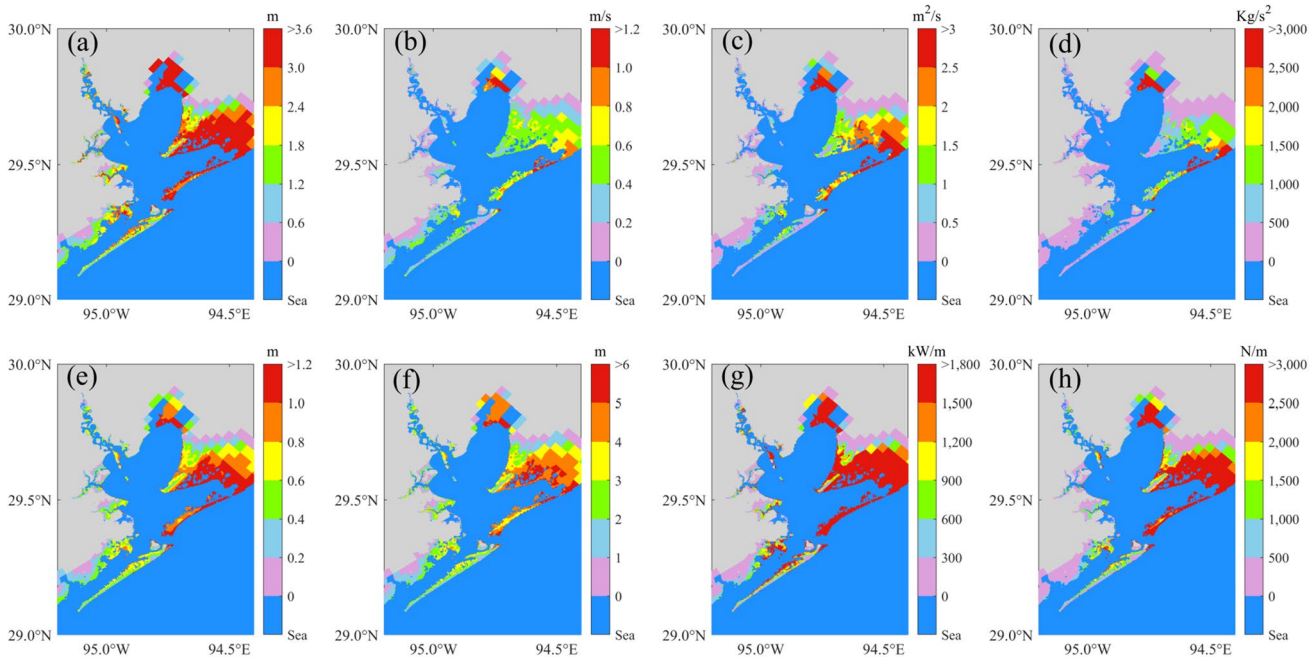

Fig. 8 The maximum values of eight hydrodynamic parameters. **a** Water depth; **b** flow velocity; **c** unit discharge; **d** flow momentum flux; **e** significant wave height; **f** Total water depth; **g** wave energy; **h** total force

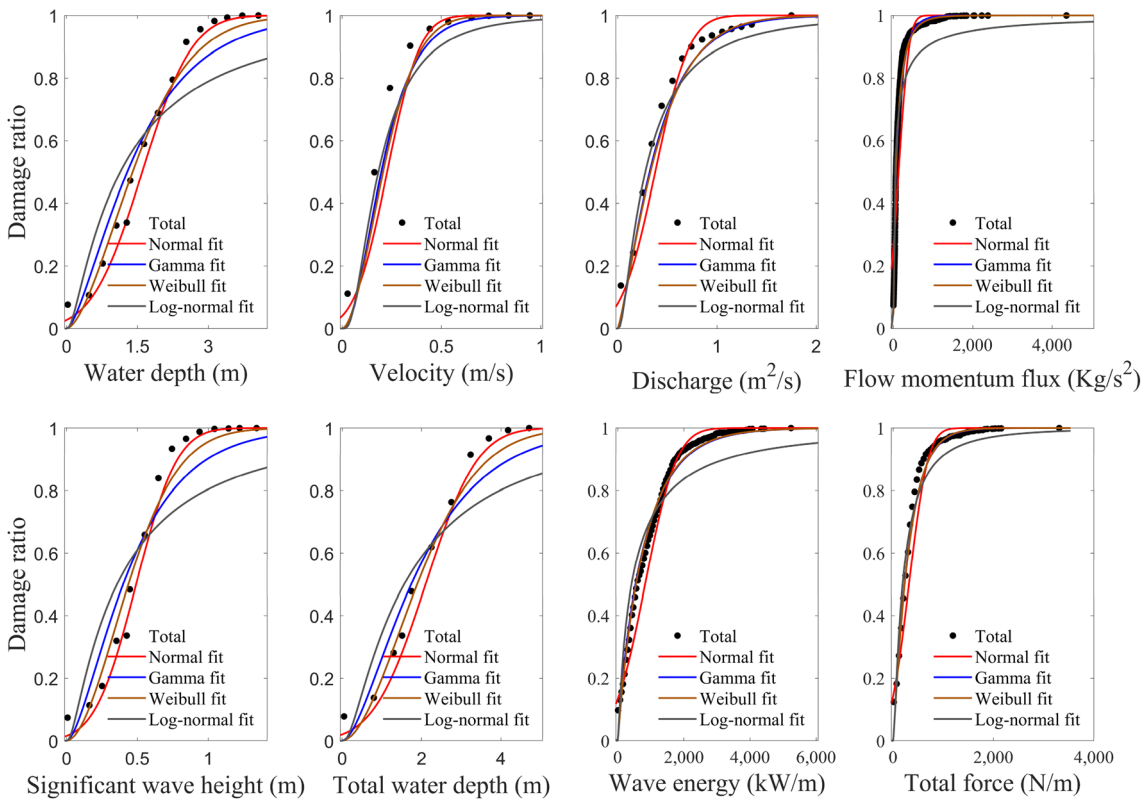

Fig. 9 Damage curves for each hydrodynamic parameter

Table 2 Goodness-of-fit indices for the normal, gamma, Weibull, and log-normal statistical distributions

Hydrodynamic parameters	RMSE				RRSE				ρ			
	Normal	Gamma	Weibull	Log-normal	Normal	Gamma	Weibull	Log-normal	Normal	Gamma	Weibull	Log-normal
Water depth	0.0452 m	0.0711 m	**0.0398 m**	0.1353 m	0.1331	0.2092	**0.1171**	0.3981	**0.9979**	0.9866	0.9957	0.9563
Flow velocity	0.0899 m/s	**0.0664 m/s**	0.0729 m/s	0.0689 m/s	0.3401	**0.2510**	0.2756	0.2606	0.9754	**0.9925**	0.9893	0.9925
Unit discharge	0.0645 m^2/s	**0.0473 m^2/s**	0.0500 m^2/s	0.0565 m^2/s	0.2380	**0.1745**	0.1847	0.2084	0.9877	**0.9951**	0.9944	0.9901
Flow momentum flux	0.0580 kg/s^2	0.0197 kg/s^2	**0.0177 kg/s^2**	0.0691 kg/s^2	0.4646	0.1574	**0.1418**	0.5535	0.9299	0.9875	**0.9902**	0.9576
Significant wave height	**0.0442 m**	0.0899 m	0.0504 m	0.1596 m	**0.1238**	0.2517	0.1411	0.4472	**0.9978**	0.9796	0.9926	0.9464
Total water depth	0.0542 m	0.0756 m	**0.0464 m**	0.1331 m	0.1582	0.2210	**0.1354**	0.3889	**0.9975**	0.9858	0.9961	0.9544
Wave energy flux	0.0465 kW/m	0.0247 kW/m	**0.0222 kW/m**	0.0807 kW/m	0.1911	0.1014	**0.0912**	0.3315	0.9912	0.9962	**0.9965**	0.9802
Total force	0.0594 N/m	**0.0262 N/m**	0.0265 N/m	0.0491 N/m	0.2660	**0.1173**	0.1187	0.2201	0.9773	0.9950	**0.9951**	0.9870

RMSE root mean square error, *RRSE* relative root square error, and ρ is the Pearson correlation coefficient
The bold indicates that it is the best fitting function

found that more than 50% of the damage occurs in the first 1.5 m of flood depth and more than 90% of the damage occurs in the first 3 m of flood depth, which is similar to previous studies (Ruangrassamee et al. 2006; Reese and Ramsay 2010; Suppasri et al. 2013; Diaz-Loaiza et al. 2022).

3.4 Effect of Number of Stories and Building Elevation

Pile-elevated coastal residences are common along Galveston Bay, and a study by Tomiczek et al. (2013) showed a strong influence of structural elevation on the damage to coastal residences. Meanwhile, the design of load bearing elements of residential construction differs for different numbers of stories; therefore, the number of stories also affects the resistance of the building to external forcing (Suppasri et al. 2013). The NFIP database reports whether or not buildings are elevated, and whether each building has 1, 2, or 3 or more stories. We therefore divided the NFIP data into six groups: 1 story elevated, 2 stories elevated, 3 stories elevated, 1 story not elevated, 2 stories not elevated, and 3 stories not elevated, and then built the damage curves for these six groups according to the method in Sect. 3.3. Figure 10 shows that, except for total water depth, the other seven hydrodynamic parameters had the same trend. For the elevated buildings, the damage curves gradually shift downward with an increase in the number of stories, while the non-elevated buildings have the opposite trend, and these damage curves gradually shift upward with an increase in the number of stories. The damage curves of elevated buildings of three stories and above are the lowest, while the damage curves of non-elevated buildings of three stories and above are the highest, and the damages are the most serious. The damage curves of the other four groups show less difference, are located between the first two damage curves, and have similar trends.

4 Discussion

In this section, we analyze how damage curves respond to model resolution, discuss their characteristics, compare them with similar damage curves worldwide, and assess their policy implications.

4.1 Sensitivity of Damage Curves to Model Resolution

The resolution of topographic data has been shown to have a significant impact on hydrodynamic results and the fitting of damage curves (Veeramony et al. 2017; Diaz-Loaiza et al. 2022). The grid resolution also has an impact on the results of the model, and a suitable grid resolution

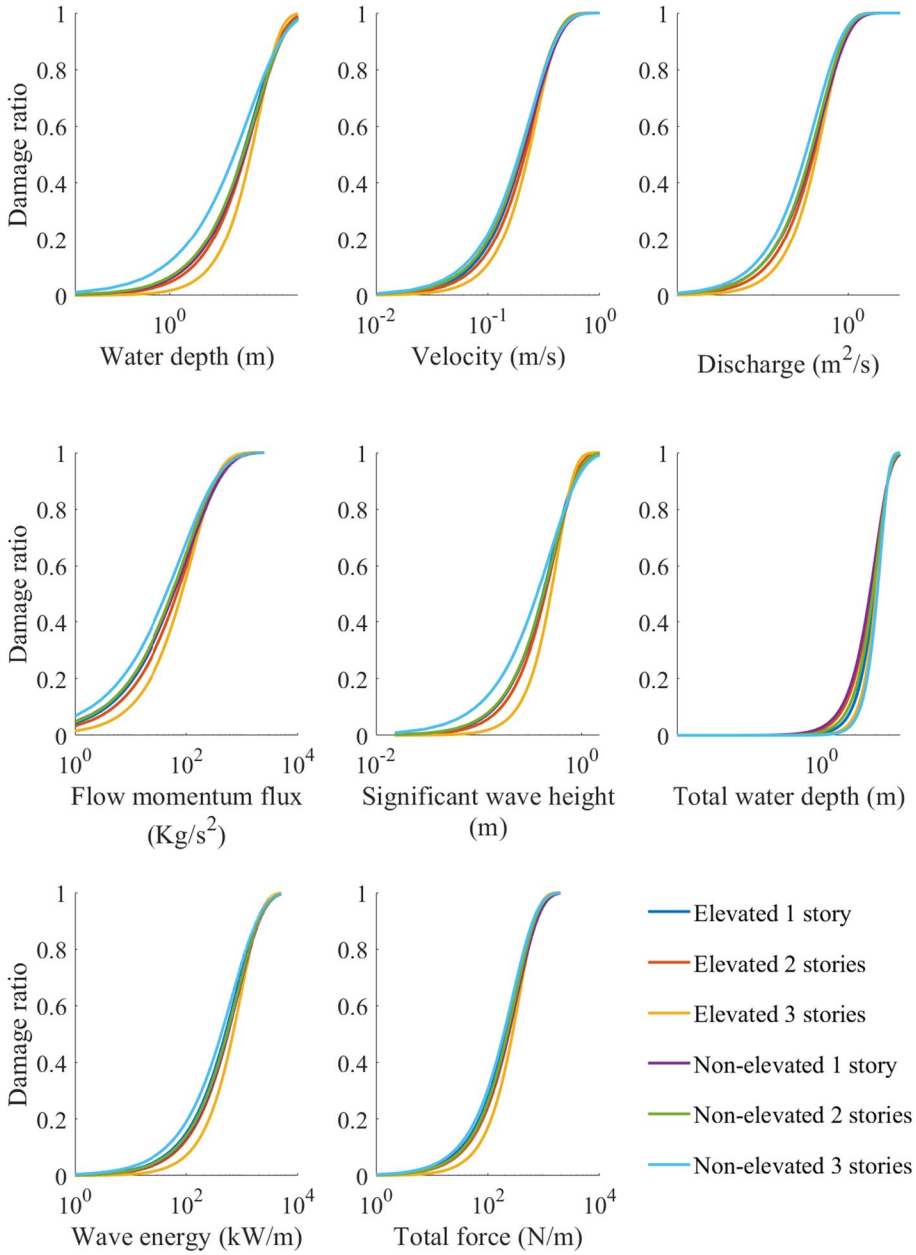

Fig. 10 Damage curves for each hydrodynamic parameter, discriminating based on elevation and number of stories

needs to be selected for the simulation (Al-Attabi et al. 2023). Inspired by this, sensitivity tests were conducted to analyze the effect of different grid resolutions on the fitting of damage curves in this study. We designed four grid resolutions (50 m, 100 m, 200 m, and 400 m) to analyze the relationship between water depth and DR, taking water depth as an example. As shown in Fig. 11, starting from 400 m, the damage curve gradually shifts upward as the grid resolution increases. When the grid resolution reaches 50 m, the result is almost equivalent to 100 m resolution. This is because the claim locations are located on land, but when the grid resolution is coarse, some claim locations on the shoreline (such as beach houses) are simulated as in the sea, so the modeled hazards at these claim locations are outliers and are not counted in the statistics. Meanwhile, from the results of Sect. 3.1, we know that this shoreline region contained many locations with high DR. In summary, the low-resolution grid ignores some claim locations with high DR, resulting in a lower damage curve. Given that the 100 m grid accurately represented the main topographical features, such as shoreline location and navigation channels, increasing the resolution to 50 m did not meaningfully alter the results of the damage curves. However, this increase in resolution substantially increased computational expense. Therefore, in this study, the grid resolution of the study area is set at 100 m.

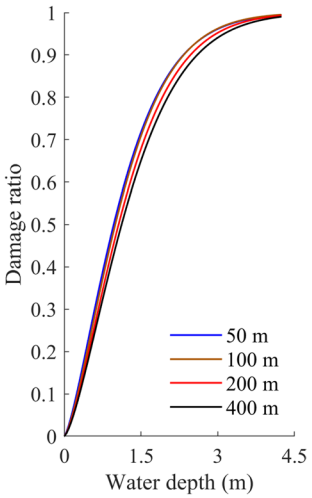

Fig. 11 Damage curves as a function of water depth, with different grid resolutions

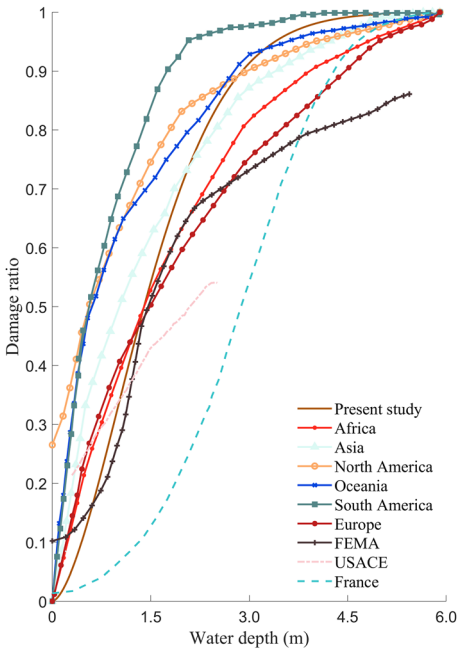

Fig. 12 Comparison of damage curves for water depth in different regions of the world. The data of Africa, Asia, North America, Oceania, South America, and Europe are from Huizinga et al. (2017); FEMA data are from Tomiczek et al. (2013); USACE data are from Wing et al. (2020); France data are from Diaz-Loaiza et al. (2022).

4.2 Analysis of the Damage Curve

Fewer residential structures in northeast Texas City suffered damage (Fig. 7), but this area along the coast was not affected by a strong inundation during the hurricane due to its coastal revetment, which is like a fixed weir (Fig. 8). In Sect. 3.4 we can see that a building elevation has a significant impact on the ability of the building to resist damage. The non-elevated buildings experienced more damage as the number of stories increased, probably because the DR in this study was derived from the NFIP insurance database determined by the replacement cost of the building, and higher buildings cost more to (re)build than lower buildings. During a hurricane of this magnitude, most of the western Galveston Bay coastal area was inundated by 0.6–3.6 m of water (Fig. 8a), which is already at a depth that has been seen to cause moderate to severe damage (Ruangrassamee et al. 2006; Suppasri et al. 2013; Fuchs et al. 2019; Diaz-Loaiza et al. 2022). Non-elevated buildings are affected by hydrodynamic forces and the impact of floating debris, incurring higher repair costs. Elevated buildings are relatively less affected by hydrodynamic forces due to their distance from the ground, and the required repair costs are lower than those of non-elevated buildings when the strong resistance of multiple stories is more prominent. Thus, elevated buildings experience less damage as the number of stories increases. Also, the overall damage curves of elevated buildings are lower than that of non-elevated buildings.

It is well-documented that insurance claims can be susceptible to fraud or misinformation (Diaz-Loaiza et al. 2022). Furthermore, factors related to asset vulnerability, such as construction characteristics, materials used, quality, and structure age (Suppasri et al. 2013; Paprotny et al. 2020), play crucial roles in determining the extent to which a specific hydrodynamic variable is associated with damage. This introduces an additional layer of complexity to the analysis. Moreover, it is noteworthy that if more detailed information from the claims data were accessible, such as structure type, structure age, and damage stage, it would enable the generation of more intricate fragility functions. Finally, the maximum limit of the NFIP coverage is up to USD 250,000 for buildings and USD 100,000 for content (Kousky 2018). Hence, the dollar amount of building claim (a measure of loss) may be underreporting sustained structural damages for buildings with the value exceeding USD 250,000. More accurate damage assessment at the structure level will certainly improve the reliability of damage curve estimates.

4.3 Comparison with Other Global Damage Curves

A comparison of building damage curves with previous findings can be made using water depth as an example. A summary of building damage curves from many locations (Tomiczek et al. 2013; Huizinga et al. 2017; Wing et al. 2020; Diaz-Loaiza et al. 2022) is shown in Fig. 12. The damage curve in Galveston Bay is characterized by two regions compared to other damage curves. When the water depth is below about 1.5 m, the damage curve in this area is lower than most of the others. When the water depth exceeds 1.5 m, the slope of the

Galveston Bay damage curve increases sharply. DR exceeds 90% at about 3 m. This is because when the water depth is low, this region has a lower DR than other regions of the world due to the presence of elevated buildings.

4.4 Policy Implications

This study has highlighted the importance of structural elevation for coastal hazard mitigation as the overall damage curves of elevated buildings are found to be lower than that of non-elevated buildings. Structural elevation requirements are tied to standards put forth by the NFIP to protect against a 1%-annual-chance flood or 100-year flood. Location-specific base flood elevation requirements (BFE), designated by FEMA Flood Insurance Rate Maps (FIRMs), are the minimum standard for elevation of new, substantially damaged, or improved structure construction. Communities are encouraged to set elevation requirements above the BFE standards, and certain classes of Community Rating System communities, working to receive credit toward discounted flood insurance premiums, must adopt freeboard requirements above the BFE (FEMA 2020). Elevation above NFIP 100-year floodplain requirements is increasingly important as extreme weather events and studies have revealed flooding outside of the 100-year floodplain (Brody and Highfield 2011; Highfield et al. 2013; Brody et al. 2014; Blessing et al. 2017; Rainey et al. 2021), and climate change is intensifying heavy precipitation events (Tabari 2020). Research has long established that flood damage is decreased with adoption of freeboard standards (Godschalk et al. 1989; Highfield et al. 2014), and coastal residents have been found to be supportive of elevation. In a study of Upper Texas coastal residents, including those of Galveston Island, Ross and Atoba (2022) found that structural elevation is the most supported hazard mitigation strategy with 65% of the survey respondents saying they "support a lot" this strategy. The issue in widespread policy adoption of higher standards for elevation, therefore, is improved knowledge of future climate risk to determine just how high structures should be. Current floodplain maps and elevation standards are based on historic data; they do not factor in sea level rise and changing climate conditions (Pralle 2019). Updates to NFIP risk rating methodology are making only incremental improvements by including additional (historic) flood variables (FEMA n.d.). Until flood maps account for future flood risk, minimum elevation standards will fail to provide the protection needed (Pralle 2019).

5 Conclusion

In this study, we simulated storm surges and waves from Hurricane Ike, which impacted Galveston Bay in September 2008. Comparisons of water level, significant wave height, peak wave period, and inundation depth with multiple observations confirm that the model performed effectively in hindcasting the flow and wave processes during this event. We then generated damage curves for this region using eight modeled hydrodynamic parameters and DRs derived from NFIP data using the Weibull cumulative distribution function. We have thus drawn the following conclusions:

- About 50% of the damage occurs in the first 1.5 m of flood depth and about 90% of the damage occurs in the first 3 m of flood depth.
- The damage curve becomes higher as the grid resolution increases, but stabilizes when the resolution reaches 100 m.
- The damage curves of elevated buildings in this area decrease with a greater number of stories and are lower than the damage curves of non-elevated buildings. The damage curves of non-elevated buildings show the opposite trend, increasing with an increase in the number of stories. Therefore, elevated buildings have an important influence on the resistance of buildings to damage during hurricanes.
- Compared to other depth-damage functions from the literature, the depth-damage curve for Galveston Bay predicts a lower DR for inundation depth less than 1.5 m, but a higher DR for inundation depth greater than 1.5 m.

The current study considers only monovariate damage curves, applying only 1 forcing variable at a time. Future work can include multivariate damage analysis, investigating the correlation of damage with many forcing variables using machine learning (Nateghi et al. 2016).

Acknowledgments This research was funded by NSF award 2228486 under the program Strengthening America's Infrastructure. Chaoran Xu acknowledges funding from the China Scholarship Council, Grant No. 202206140090.

References

Al-Attabi, Z., Y. Xu, G. Tso, and S. Narayan. 2023. The impacts of tidal wetland loss and coastal development on storm surge damages

to people and property: A Hurricane Ike case-study. *Scientific Reports* 13(1): Article 4620.

Berg, R. 2009. *Tropical cyclone report Hurricane Ike*. Miami, FL: National Hurricane Center.

Blessing, R., A. Sebastian, and S.D. Brody. 2017. Flood risk delineation in the United States: How much loss are we capturing?. *Natural Hazards Review*. https://doi.org/10.1061/(ASCE)NH.1527-6996.0000242.

Brody, S.D., and W.E. Highfield. 2011. Evaluating the effectiveness of the FEMA community rating system in reducing flood losses. Final Rep. for FEMA Mitigation Division Study, Phase I, National Institute of Building Sciences, Washington, DC.

Brody, S., R. Blessing, A. Sebastian, and P. Bedient. 2014. Examining the impact of land use/land cover characteristics on flood losses. *Journal of Environmental Planning and Management* 57(8): 1252–1265.

Bricker, J.D., M. Esteban, H. Takagi, and V. Roeber. 2017. Economic feasibility of tidal stream and wave power in post-Fukushima Japan. *Renewable Energy* 114: 32–45.

Bunya, S., J.C. Dietrich, J.J. Westerink, B.A. Ebersole, J.M. Smith, J.H. Atkinson, R. Jensen, D.T. Resio, et al. 2010. A high-resolution coupled riverine flow, tide, wind, wind wave, and storm surge model for Southern Louisiana and Mississippi. Part I: Model development and validation. *Monthly Weather Review* 138(2): 345–377.

Davlasheridze, M., K.O. Atoba, S. Brody, W. Highfield, W. Merrell, B. Ebersole, A. Purdue, and R.W. Gilmer. 2019. Economic impacts of storm surge and the cost-benefit analysis of a coastal spine as the surge mitigation strategy in Houston-Galveston area in the USA. *Mitigation and Adaptation Strategies for Global Change* 24(3): 329–354.

Davlasheridze, M., Q. Fan, W. Highfield, and J. Liang. 2021. Economic impacts of storm surge events: Examining state and national ripple effects. *Climatic Change* 166(1–2): Article 11.

De Risi, R., K. Goda, T. Yasuda, and N. Mori. 2017. Is flow velocity important in tsunami empirical fragility modeling?. *Earth Science Reviews* 166: 64–82.

Deltares. 2022a. D-flow flexible mesh. Computational cores and user interface. User manual. Released for Delft3D FM Suite 2D3D 2022. Version 2022.02, SVN Revision 75614. https://oss.deltares.nl/web/delft3dfm/manuals. Accessed 16 Apr 2023.

Deltares. 2022b. D-waves simulation of short-crested waves with SWAN user manual. Version 1.2, SVN Revision 75624. https://oss.deltares.nl/web/delft3dfm/manuals. Accessed 16 Apr 2023.

Demuth, J.L., M. DeMaria, and J.A. Knaff. 2006. Improvement of advanced microwave sounding unit tropical cyclone intensity and size estimation algorithms. *Journal of Applied Meteorology and Climatology* 45(11): 1573–1581.

Diaz-Loaiza, M.A., J.D. Bricker, R. Meynadier, T.M. Duong, R. Ranasinghe, and S.N. Jonkman. 2022. Development of damage curves for buildings near La Rochelle during storm Xynthia based on insurance claims and hydrodynamic simulations. *Natural Hazards and Earth System Sciences* 22(2): 345–360.

Egbert, G.D., and S.Y. Erofeeva. 2002. Efficient inverse modeling of barotropic ocean tides. *Journal of Atmospheric and Oceanic Technology* 19(2): 183–204.

Englhardt, J., H. de Moel, C.K. Huyck, M.C. de Ruiter, J.C.J.H. Aerts, and P.J. Ward. 2019. Enhancement of large-scale flood risk assessments using building-material-based vulnerability curves for an object-based approach in urban and rural areas. *Natural Hazards and Earth System Sciences* 19(8): 1703–1722.

FEMA (Federal Emergency Management Agency). 2020. NFIP's community rating system (CRS) class 8 freeboard prerequisite. https://crsresources.org/files/2021-addendum/class_8_freeboard_faq.pdf. Accessed 10 May 2023.

FEMA (Federal Emergency Management Agency). 2023. FIMA NFIP redacted claims data set. Hyattsville, MD: FEMA.

Franklin, J.L., and C.W. Landsea. 2013. Atlantic hurricane database uncertainty and presentation of a new database format. *Monthly Weather Review* 141(10): 3576–3592.

Fuchs, S., M. Heiser, M. Schlögl, A. Zischg, M. Papathoma-Köhle, and M. Keiler. 2019. Short communication: A model to predict flood loss in mountain areas. *Environmental Modelling & Software* 117: 176–180.

Godschalk, D.R., D.J. Brower, and T. Beatley. 1989. *Catastrophic coastal storms: Hazard mitigation and development management*. Durham: Duke University Press.

Hatzikyriakou, A., and N. Lin. 2018. Assessing the vulnerability of structures and residential communities to storm surge: An analysis of flood impact during Hurricane Sandy. *Frontiers in Built Environment* 4: Article 4.

HCFCD (Harris County Flood Control District). 2009. Hurricane Ike inundation depth. https://www.hcfcd.org/About/Harris-Countys-Flooding-History/Hurricane-Ike-2008. Accessed 9 May 2023.

Highfield, W.E., S.A. Norman, and S.D. Brody. 2013. Examining the 100-year floodplain as a metric of risk, loss, and household adjustment. *Risk Analysis* 33(2): 86–191.

Highfield, W.E., S.D. Brody, and R. Blessing. 2014. Measuring the impact of mitigation activities on flood loss reduction at the parcel level: The case of the clear creek watershed on the upper Texas coast. *Natural Hazards* 74: 687–704.

Holland, G. 2008. A revised hurricane pressure-wind model. *Monthly Weather Review* 136(9): 3432–3445.

Holland, G.J., J.I. Belanger, and A. Fritz. 2010. A revised model for radial profiles of hurricane winds. *Monthly Weather Review* 138(12): 4393–4401.

Huizinga, J., H.D. Moel, and W. Szewczyk. 2017. *Global flood depth-damage functions*. Luxembourg: Publications Office of the European Union.

Ichii, K. 2002. A seismic risk assessment procedure for gravity type quay walls. *Structural Engineering/Earthquake Engineering* 19(2): 131–140.

Jansen, L., P.A. Korswagen, J.D. Bricker, S. Pasterkamp, K.M. de Bruijn, and S.N. Jonkman. 2020. Experimental determination of pressure coefficients for flood loading of walls of Dutch terraced houses. *Engineering Structures* 216: Article 110647.

Ke, Q., J.S. Yin, J.D. Bricker, N. Savage, E. Buonomo, Q.H. Ye, P. Visser, and G.T. Dong et al. 2021. An integrated framework of coastal flood modelling under the failures of sea dikes: A case study in Shanghai. *Natural Hazards* 109(1): 671–703.

Knutson, T., S.J. Camargo, J.C.L. Chan, K. Emanuel, C.-H. Ho, J. Kossin, M. Mohapatra, and M. Satoh et al. 2019. Tropical cyclones and climate change assessment: Part I: Detection and attribution. *Bulletin of the American Meteorological Society* 100(10): 1987–2007.

Kousky, C. 2018. Financing flood losses: A discussion of the National Flood Insurance Program. *Risk Management and Insurance Review* 21(1): 11–32.

Kreibich, H., K. Piroth, I. Seifert, H. Maiwald, U. Kunert, J. Schwarz, B. Merz, and A.H. Thieken. 2009. Is flow velocity a significant parameter in flood damage modelling?. *Natural Hazards and Earth System Sciences* 9(5): 1679–1692.

Li, L., and P. Chakraborty. 2020. Slower decay of landfalling hurricanes in a warming world. *Nature* 587(7833): 230–234.

Makin, V.K. 2005. A note on the drag of the sea surface at hurricane winds. *Boundary-Layer Meteorology* 115: 169–176.

Masoomi, H., J.W. van de Lindt, M.R. Ameri, T.Q. Do, and B.M. Webb. 2019. Combined wind-wave-surge hurricane-induced damage prediction for buildings. *Journal of Structural Engineering* 145(1): Article 04018227.

Mendelsohn, R., K. Emanuel, S. Chonabayashi, and L. Bakkensen. 2012. The impact of climate change on global tropical cyclone damage. *Nature Climate Change* 2(3): 205–209.

Muis, S., M. Verlaan, H.C. Winsemius, J.C.J.H. Aerts, and P.J. Ward. 2016. A global reanalysis of storm surges and extreme sea levels. *Nature Communications* 7(1): 11969–11969.

Nateghi, R., J.D. Bricker., S.D. Guikema, and A. Bessho. 2016. Statistical analysis of the effectiveness of seawalls and coastal forests in mitigating tsunami impacts in Iwate and Miyagi Prefectures. *PLoS ONE* 11(8): Article e0158375.

Nederhoff, K., A. Giardino, M.V. Ormondt, and D. Vatvani. 2019. Estimates of tropical cyclone geometry parameters based on best-track data. *Natural Hazards and Earth System Sciences* 19(11): 2359–2370.

NOAA (National Oceanic and Atmospheric Administration). 2023. Most expensive natural disasters in the United States as of December 2022 (in billion U.S. dollars). https://www.statista.com/statistics/744015/most-expensive-natural-disasters-usa/. Accessed 9 May 2023.

Oliver-Smith, A. 2009. Sea level rise and the vulnerability of coastal peoples: Responding to the local challenges of global climate change in the 21st century. Bonn, Germany: UNU-EHS.

Overpeck, S. 2009. Hurricane Ike wind analysis for southeast Texas. Dickinson, Texas: National Oceanic and Atmospheric Administration and National Weather Service. https://www.weather.gov/hgx/projects_ike08_wind_analysis. Accessed 10 Apr 2023.

Paprotny, D., H. Kreibich, O. Morales-Nápoles, D. Wagenaar, A. Castellarin, F. Carisi, X. Bertin, B. Merz, and K. Schröter. 2020. A probabilistic approach to estimating residential losses from different flood types. *Natural Hazards* 105(3): 2569–2601.

Pistrika, A.K., and S.N. Jonkman. 2009. Damage to residential buildings due to flooding of New Orleans after hurricane Katrina. *Natural Hazards* 54(2): 413–434.

Postacchini, M., G. Zitti, E. Giordano, F. Clementi, G. Darvini, and S. Lenci. 2019. Flood impact on masonry buildings: The effect of flow characteristics and incidence angle. *Journal of Fluids and Structures* 88: 48–70.

Pralle, S. 2019. Drawing lines: FEMA and the politics of mapping flood zones. *Climatic Change* 152(2): 227–237.

Rainey, J.L., S.D. Brody, G.E. Galloway, and W.E. Highfield. 2021. Assessment of the growing threat of urban flooding: A case study of a national survey. *Urban Water Journal* 18(5): 375–381.

Reed, D., Y.S. Wang, E. Meselhe, and E. White. 2020. Modeling wetland transitions and loss in coastal Louisiana under scenarios of future relative sea-level rise. *Geomorphology* 352: Article 106991.

Reese, S., and D. Ramsay. 2010. RiskScape: Flood fragility methodology. Technical report WLG2010-45. https://www.wgtn.ac.nz/sgees/research-centres/documents/riskscape-flood-fragility-methodology.pdf. Accessed 10 May 2023.

Ross, A.D., and K.O. Atoba. 2022. The dimensions of individual support for coastal hazard mitigation: Analysis of a survey of Upper Texas coast residents. *Natural Hazards Review* 23(2): 04022004.

Ruangrassamee, A., H. Yanagisawa, P. Foytong, P. Lukkunaprasit, S. Koshimura, and F. Imamura. 2006. Investigation of tsunami induced damage and fragility of buildings in Thailand after the December 2004 Indian Ocean Tsunami. *Earthquake Spectra* 22(3): 377–401.

Sampson, C.C., A.M. Smith, P.D. Bates, J.C. Neal, L. Alfieri, and J.E. Freer. 2015. A high-resolution global flood hazard model. *Water Resource Research* 51(9): 7358–7381.

Sebastian, A., J. Proft, J.C. Dietrich, W. Du, P.B. Bedient, and C.N. Dawson. 2014. Characterizing hurricane storm surge behavior in Galveston Bay using the SWAN+ADCIRC model. *Coastal Engineering* 88: 171–181.

Shinozuka, M., M.Q. Feng, J. Lee, and T. Naganuma. 2000. Statistical analysis of fragility curves. *Journal of Engineering Mechanics* 126(12): 1224–1231.

Suppasri, A., E. Mas, I. Charvet, R. Gunasekera, K. Imai, Y. Fukutani, Y. Abe, and F. Imamura. 2013. Building damage characteristics based on surveyed data and fragility curves of the 2011 Great East Japan tsunami. *Natural Hazards* 66(2): Article 319341.

Tabari, H. 2020. Climate change impact on flood and extreme precipitation increases with water availability. *Scientific Reports* 10(1): 1–10.

Takagi, H., and W. Wu. 2016. Maximum wind radius estimated by the 50 kt radius: Improvement of storm surge forecasting over the western North Pacific. *Natural Hazards and Earth System Sciences* 16(3): 705–717.

Tomiczek, T., A. Kennedy, and S. Rogers. 2013. Survival analysis of elevated homes on the Bolivar Peninsula after Hurricane Ike. In *Advances in hurricane engineering: Learning from our past*, ed. C.P. Jones, and L.G. Griffis, 108–118. Reston, VA: American Society of Civil Engineers.

Tomiczek, T., A. Kennedy, Y. Zhang, M. Owensby, M.E. Hope, N. Lin, and A. Flory. 2017. Hurricane damage classification methodology and fragility functions derived from Hurricane Sandy's effects in coastal New Jersey. *Journal of Waterway, Port, Coastal, and Ocean Engineering* 143(5): Article 04017027.

Törnqvist, T.E., D.R. Cahoon, J.T. Morris, and J.W. Day. 2021. Coastal wetland resilience, accelerated sea-level rise, and the importance of timescale. *AGU Advances* 2(1): Article e2020AV000334.

Totschnig, R., and S. Fuchs. 2013. Mountain torrents: Quantifying vulnerability and assessing uncertainties. *Engineering Geology* 155: 31–44.

Tsubaki, R., J.D. Bricker, K. Ichii, and Y. Kawahara. 2016. Development of fragility curves for railway embankment and ballast scour due to overtopping flood flow. *Natural Hazards and Earth System Sciences* 16(12): 2455–2472.

Tyler, J., A.-A. Sadiq, D.S. Noonan, and R.M. Entress. 2021. Decision making for managing community flood risks: Perspectives of United States floodplain managers. *International Journal of Disaster Risk Science* 14(5): 649–660.

Veeramony, J., A.J. Condon, R.S. Linzell, and K. Watson. 2016. Validation of Delft3D as a coastal surge and inundation prediction system. Stennis Ste, MS: Naval Research Lab Stennis Detachment Stennis Space Center.

Veeramony, J., A. Condon, and M.V. Ormondt. 2017. Forecasting storm surge and inundation: Model validation. *Weather and Forecasting* 32(6): 2045–2063.

Wing, O.E.J., N. Pinter, P.D. Bates, and C. Kousky. 2020. New insights into US flood vulnerability revealed from flood insurance big data. *Nature Communications* 11(1): Article 1444.

Winsemius, H.C., J.C.J.H. Aerts, L.P.H. van Beek, M.F.P. Bierkens, A. Bouwman, B. Jongman, J.C.J. Kwadijk, and W. Ligtvoet et al. 2015. Global drivers of future river flood risk. *Nature Climate Change* 6(4): 381–385.

Xu, H.Q., Z. Tian, L.X. Sun, Q.H. Ye, E. Ragno, J. Bricker, G.Q. Mao, and J.K. Tan et al. 2022. Compound flood impact of water level and rainfall during tropical cyclone periods in a coastal city: The case of Shanghai. *Natural Hazards and Earth System Sciences* 22(7): 2347–2358.

Xu, C.R., Y. Yang, F. Zhang, R.Z. Li, Z.H. Li, Y.P. Wang, and J.J. Jia. 2022. Spatial-temporal distribution of tropical cyclone activity on the eastern sea area of China since the late 1940s. *Estuarine, Coastal and Shelf Science* 277(31): Article 208067.

Zhang, L., and V.P. Singh. 2005. Frequency analysis of flood damage. *Journal of Hydrologic Engineering* 10(2): 100–109.

Zou, P.X., J.D. Bricker, and W.S.J. Uijttewaal. 2020. Impacts of extreme events on hydrodynamic characteristics of a submerged floating tunnel. *Ocean Engineering* 218: Article 108221.